PNAS RESEARCH ARTICLE | CHEMISTRY

Radius measurement via super-resolution microscopy enables the development of a variable radii proximity labeling platform

James V. Oakley[a,b,1], Benito F. Buksh[a,b,1], David F. Fernández[a,b], Daniel G. Oblinsky[b], Ciaran P. Seath[a,b], Jacob B. Geri[a,b], Gregory D. Scholes[b], and David W. C. MacMillan[a,b,2]

Edited by Stephen Benkovic, The Pennsylvania State University, University Park, PA; received February 18, 2022; accepted June 23, 2022

The elucidation of protein interaction networks is critical to understanding fundamental biology as well as developing new therapeutics. Proximity labeling platforms (PLPs) are state-of-the-art technologies that enable the discovery and delineation of biomolecular networks through the identification of protein-protein interactions. These platforms work via catalytic generation of reactive probes at a biological region of interest; these probes then diffuse through solution and covalently "tag" proximal biomolecules. The physical distance that the probes diffuse determines the effective labeling radius of the PLP and is a critical parameter that influences the scale and resolution of interactome mapping. As such, by expanding the degrees of labeling resolution offered by PLPs, it is possible to better capture the various size scales of interactomes. At present, however, there is little quantitative understanding of the labeling radii of different PLPs. Here, we report the development of a superresolution microscopy-based assay for the direct quantification of PLP labeling radii. Using this assay, we provide direct extracellular measurements of the labeling radii of state-of-the-art antibody-targeted PLPs, including the peroxidase-based phenoxy radical platform (269 ± 41 nm) and the high-resolution iridium-catalyzed μMap technology (54 ± 12 nm). Last, we apply these insights to the development of a molecular diffusion-based approach to tuning PLP resolution and introduce a new aryl-azide-based μMap platform with an intermediate labeling radius (80 ± 28 nm).

proximity labeling | photoredox catalysis | STED microscopy

Significance

Proximity labeling platforms (PLPs) are biochemical techniques that have attracted significant interest for their ability to map biological interaction networks, or interactomes, thus expanding our understanding of biology and providing therapeutic insight. However, the spatial resolution of PLPs, a critical parameter that influences the accuracy of identified interactomes, remains largely unknown. Using super-resolution microscopy, we have obtained direct extracellular measurements of various PLP labeling radii. We then used this assay to develop a novel PLP with an unprecedented spatial resolution, expanding the available PLP toolkit for biological discovery.

Nearly all cellular processes are governed by physical interactions between biomolecules. Consequently, these biomolecular associations directly underlie many pathologies, and elucidating their role in disease pathways can directly inform therapeutic discovery. As one example, the identification of critical disease-related protein-protein interactions (PPIs) has led to the development of novel treatments for several cancers (1–6), viral infections (7–9), and inflammatory disorders (9–11). Accordingly, a central goal across all biology remains the development of technologies that are capable of identifying such biological interaction networks, or interactomes.

Over the past decade, proximity labeling platforms (PLPs) have emerged as state-of-the-art technologies for mapping biomolecular interactomes (12). PLPs function by first localizing an enzyme or small-molecule catalyst to a known protein of interest (POI) within a target interactome (Fig. 1*A*). This catalyst then converts an inert proximity labeling probe into a reactive species, which then diffuses away from its site of activation and covalently crosslinks with encountered biomolecules. This tag can then be used to isolate and identify labeled biomolecules to infer a close spatial relationship with the POI. The distance that an activated probe can diffuse in each PLP determines its effective labeling radius and is a critical parameter for influencing the scale, resolution, and accuracy of identified interactomes. Given that interaction networks can exist over a wide range of distance scales, ranging from organelle-wide organizations to nano-meter scale clusters, a longstanding goal remains the development of PLPs with differentiated labeling radii that can capture a range of spatial organizations (Fig. 1*B*).

Peroxidase-based PLPs, such as ascorbate peroxidase (APEX) (13), Biotinylation by Antibody Recognition (BAR) (14), Selective Proteomic Proximity Labeling Assay using Tyramide (SPPLAT) (15), and Enzyme Mediated Activation of Radical Sources (EMARS), have emerged as among the most widely used techniques for interactome mapping and have facilitated significant advances in fundamental understanding across a number of biological fields, including subcellular RNA localization (16), cell-surface interactomes (17–19), and neurobiology (20). These platforms rely on horseradish peroxidase (HRP) or APEX enzymes to activate phenol precursors into reactive phenoxy radicals in solution. In addition to the genetic encodability of these systems, the fast labeling kinetics of peroxidase are comparable with the timescales of biological processes,

Author affiliations: [a]Merck Center for Catalysis at Princeton University, Princeton, NJ 08544; and [b]Department of Chemistry, Princeton University, Princeton, NJ 08544

Author contributions: J.V.O., B.F.B., D.F.F., D.G.O., C.P.S., J.B.G., G.D.S., and D.W.C.M. designed research; J.V.O., B.F.B., D.F.F., D.G.O., and C.P.S. performed research; J.V.O., B.F.B., D.F.F., D.G.O., and C.P.S. analyzed data; and J.V.O. and D.W.C.M. wrote the paper.

Competing interest statement: A provisional U.S. patent has been filed by D.W.C.M. and C.P.S. based in part on this work, 62/982,366; 63/076,658. International Application No. PCT/US2021/019959. D.W.C.M. declares an ownership interest, C.P.S. declares an affiliation interest, in the company Dexterity Pharma LLC, which has commercialized materials used in this work. D.W.C.M. declares an ownership interest in PennPhD, which has commercialized materials used in this work.

This article is a PNAS Direct Submission.

[1]J.V.O. and B.F.B. contributed equally this work.

[2]To whom correspondence may be addressed. Email: dmacmill@princeton.edu.

This article contains supporting information online at http://www.pnas.org/lookup/suppl/doi:10.1073/pnas.2203027119/-/DCSupplemental.

Published August 1, 2022.

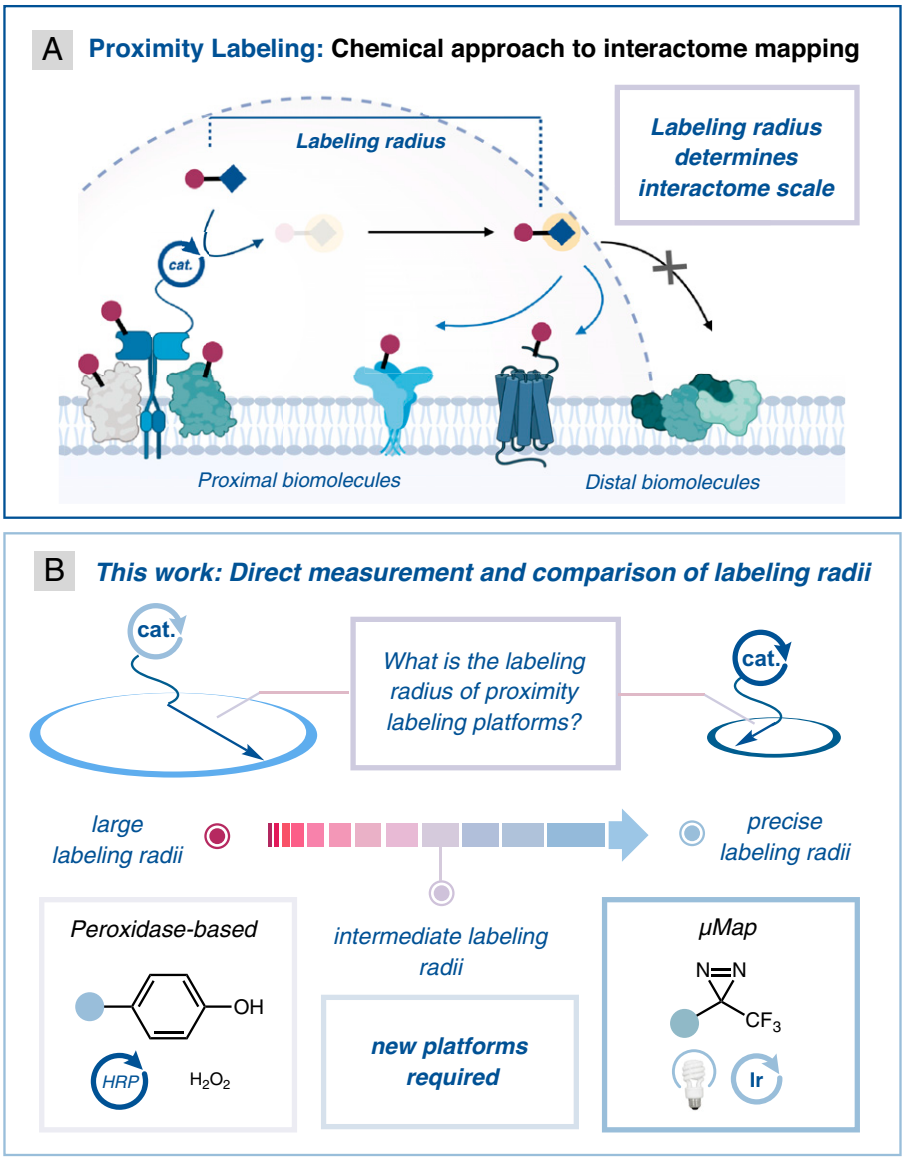

Fig. 1. (*A*) General proximity labeling regime. (*B*) State-of-the-art PLPs cover a range of spatial resolution. This work focuses on the development of a strategy for the direct measurement and comparison of state-of-the-art PLP labeling radii and the development of new PLPs with novel degrees of spatial selectivity.

and the platform has been used to obtain temporally resolved information (21, 22). However, the relatively long-lived (low millisecond) solution half-life of the phenoxy radical allows these open-shell intermediates to diffuse beyond multihundred nanometer distances in solution (23). As such, these phenoxy-based approaches can capture significant numbers of off-target biomolecules, complicating the identification of true proximal interactors (24). Conversely, PLPs with higher labeling resolution are better suited to capturing individual PPI networks that occur on a nanometer scale. To address this challenge, our laboratory has developed a light-driven PLP, which we term μMap, that is capable of high-resolution cell-surface microenvironment mapping (25). The μMap platform uses iridium photocatalysis to generate highly reactive carbenes from diazirine precursors; these carbenes serve as precise probes, labeling proximal biomolecules within a few nanometers distance or suffering rapid quenching (~2 ns) by water molecules. Targeting PD-L1 on the cell surface using photocatalyst-antibody conjugates, we have achieved selective labeling of the intercellular immune synapse, thereby demonstrating that μMap offers a higher degree of spatial resolution over peroxidase-based platforms for the mapping of cell-surface interactomes. While these results represent a qualitative improvement in spatial resolution, the precise quantitative difference remains unknown.

Together, these PLPs, in addition to other recently developed proximity labeling (PL) techniques, offer a range of spatiotemporal (26) and biomolecular (27) selectivities. However, despite the critical importance of spatial selectivity, a direct measurement and comparison of PLP labeling radii has not yet been demonstrated. Electron microscopy has been used to estimate the radius of HRP-based labeling in rat liver mitochondria (28) and APEX labeling of intermediate filaments (29); both studies suggested ~20 nm spatial labeling resolution. While these studies provide an initial estimate for labeling in the intracellular environment, this value cannot be generalized across all biological contexts, as the combination of a high concentration of radical quenchers present in the cytosol and mitochondrial matrix (30), along with macromolecular crowding (31, 32), could drastically influence spatial resolution. Honke and coworkers performed peroxidase-based EMARS labeling

on a model surface interactome, measuring a labeling radius of ~200 to 300 nm via gold immunoelectron microscopy (33); however, this study only provided a value for azido-substituted phenol probes. No direct measurement for the widely used phenol analog (HRP or APEX) has yet been performed.

Herein we report the use of super-resolution microscopy to determine the spatial resolutions of state-of-the-art proximity labeling technologies, providing direct comparisons between technologies. We further apply this method to the development of a novel PLP with a tunable labeling radius based on simple structural modification of the labeling probe. This molecular tailoring strategy should allow for a customizable approach to interactome mapping, permitting the elucidation of target biological systems of effectively any requisite scale.

Results and Discussion

To develop a method for the direct visualization and measurement of PLP labeling radii, we chose to perform dual-antibody targeted proximity labeling of the epidermal growth factor receptor (EGFR) interactome on the surface of A549 lung adenocarcinoma cells (Fig. 2*A*). Following localization of the antibody assembly to cell-surface EGFR interactomes, labeling is initiated with the addition of a biotinylated probe and an

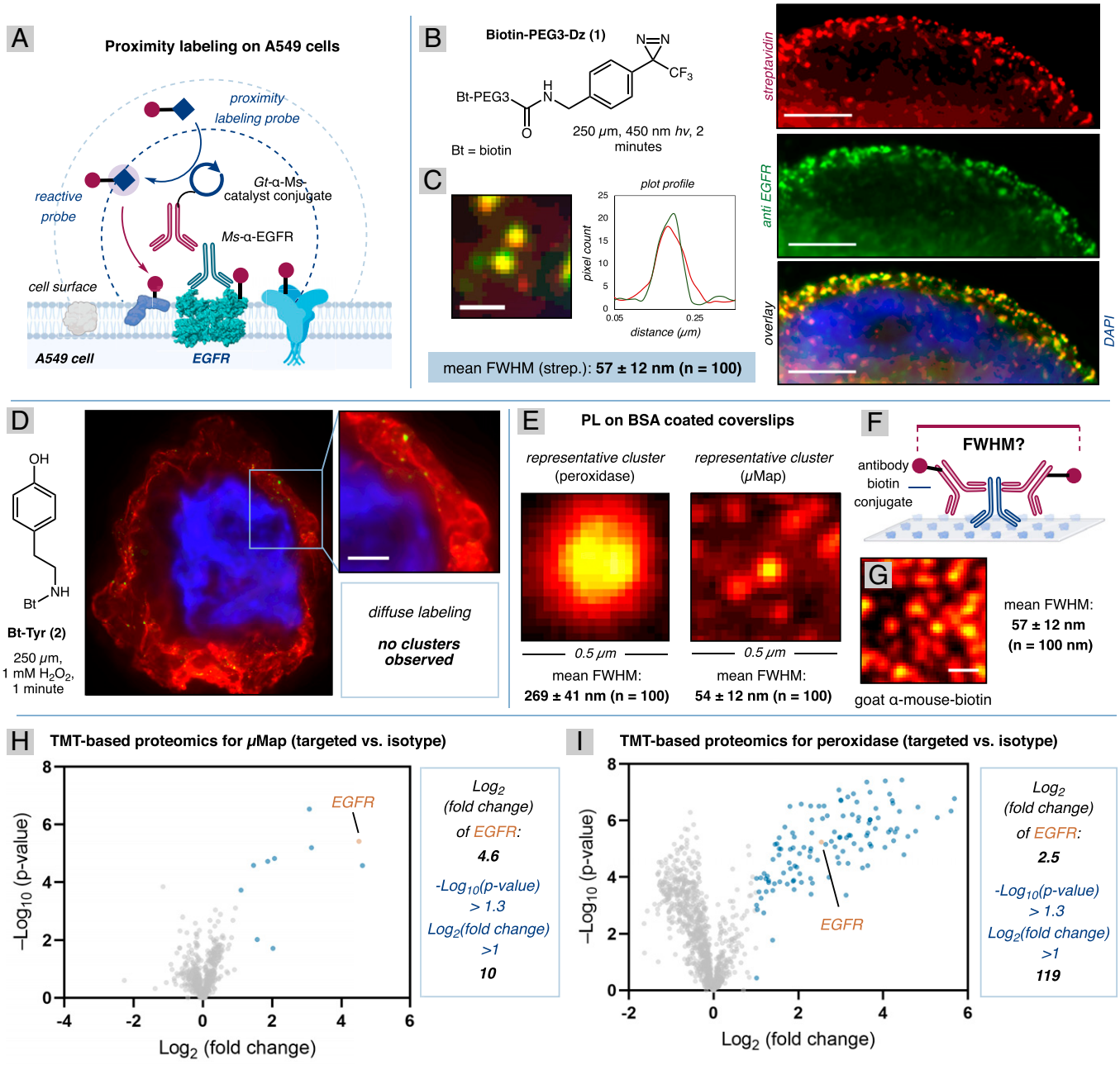

Fig. 2. (*A*) Proximity labeling of the EGFR interactome using dual antibody targeting. (*B*) STED image of radial clusters observed on the extracellular membrane of A549 cells upon μMap labeling (250 μM diazirine (**1**), 2 min irradiation). These radial clusters colocalize with EGFR (scale bar, 2 μm). (*C*) representative clusters highlighting colocalization of streptavidin and EGFR (scale bar, 200 nm). (*D*) STED image of peroxidase-based labeling (250 μM Bt-Tyr (**2**), 1 mM H_2O_2, 1 min, scale bar, 1 μm). (*E*) Measurement of peroxidase-based (*Left*, 5 mM [**2**], 1 mM H_2O_2, 15 min) and μMap (*Right*, 5 mM [**1**], 450 nm irradiation for 15 min) labeling on the surface of BSA-coated coverslips. (*F*) Biotin-antibody conjugates to probe tether-length limited hypothesis. (*G*) STED image of radial clusters observed with antibody-biotin conjugates on the coverslip surface (scale bar, 200 nm). (*H*) TMT-based proteomics of μMap labeling of EGFR on A549 cells (250 μM diazirine [**1**], 2 min irradiation). (*I*) TMT-based proteomics of peroxidase-based (250 μM Bt-Tyr [**2**], 1 mM H_2O_2, 1 min) labeling of EGFR on A549 cells.

external stimulant (oxidant or light). Streptavidin-fluorophore conjugates are then used to detect the statistical distribution of labeling events surrounding each antibody binding site. These distributions are visualized as radial clusters via fluorescence microscopy, which allows measurement of cluster size and provides a working value for the labeling radius of a given platform. Given the predicted small size of these clusters, we selected stimulated-emission depletion (STED) microscopy for this purpose, as it provides high imaging contrast and has been used to study nanometer-scale biological architectures (34, 35).

We first performed μMap labeling using biotin-diazirine probe **1** (Fig. 2*B*). Biotinylation events were captured with streptavidin STAR 635, and EGFR was costained with Alexafluor 594. Two-color STED microscopy was then used to identify colocalization. Under the μMap labeling protocol, we observed spatially resolved clusters across the cell membrane (Fig. 2*B*, streptavidin). Gratifyingly, these clusters colocalized with EGFR (Fig. 2*B*, overlay) and thus represent localized labeling events. Measurement of the streptavidin dye clusters reveals a mean full width at half maximum (FWHM) of 57 ± 12 nm (Fig. 2*C*). When a non-EGFR targeting isotype primary antibody was used, we observed clusters of EGFR but no labeling (*SI Appendix*, Fig. S1). We next examined peroxidase-based labeling using Bt-Tyr probe **2**. Strikingly, under these conditions, a diffuse distribution of streptavidin labeling was observed across the cell membrane (Fig. 2*D*). This diffuse labeling, along with the absence of defined puncta, suggests that the labeling radius of this platform lacks the spatial resolution to differentiate individual EGFR microenvironments. To obtain a measurement for the labeling radius of the peroxidase-based labeling protocol, we developed a reductionist model system, in which dual-antibody targeting PL is performed on Bovine Serum Albumin (BSA)-coated coverslips (*SI Appendix*, Fig. S2). In this model, we measured a labeling radius of 54 ± 12 nm for μMap (Fig. 2*E*), which is consistent with the value measured on the cell surface. Furthermore, we were able to resolve individual peroxidase-based proximity labeling events, measuring a mean FWHM of 269 ± 41 nm, representing an approximately fivefold larger radius than that measured for μMap under these conditions.

The reactive carbene probe generated in the μMap method has a half-life of 2 ns in aqueous solution, equating to a theoretical labeling radius of about 4 nm (36). We attribute the discrepancy between the theoretical value and the observed FWHM value of 54 nm to the length of the dual antibody assembly, which would effectively extend the labeling radius of μMap. In this regime, the labeling precision of the μMap protocol would be tether-length limited. To test this idea, we evaluated anti-mouse secondary biotin-antibody conjugate in our model BSA system, as the observed FWHM would indicate the length of the dual-antibody tether (Fig. 2*F*). We were excited to observe radial clusters of 57 ± 12 nm, a value consistent with that measured with μMap labeling on both the cell surface and the BSA-coated coverslip (Fig. 2*G*). Importantly, the absence of a quantitative difference between these systems supports a low-nm true radius for μMap labeling. Furthermore, accounting for tether length in comparing labeling radii of the μMap and HRP platforms suggests a significant (up to 200-fold) difference in precision between these two methods.

We next sought to identify the labeled cell-surface proteins in our EGFR-targeted experiments by conducting tandem-mass-tag (TMT)-based proteomics on the streptavidin-enriched proteins. From the μMap experiment, we observed 10 enriched proteins, using a cutoff of 1.0 Log_2(fold change) (Fig. 2*H*). These proteins include EGFR and three known EGFR interactors previously uncovered via affinity purification mass spectrometry: PHLDA1, LGALS1, and EPHA2 (37–42).

A similar analysis of the peroxidase-based labeling sample revealed 119 proteins enriched above 1.0 Log_2 (fold change) (Fig. 2*I*). These proteins include EGFR and 32 known interactors of EGFR previously identified through affinity capture Western or mass spectrometry (35). In contrast to the μMap dataset, wherein EGFR is the second most enriched protein, in the HRP-based experiment, EGFR is only the sixty-fourth most enriched protein. This result is consistent with the larger labeling radius of HRP on the BSA-coated coverslip and the diffuse cell-surface biotinylation pattern observed via STED microscopy. While these two platforms offer complementary spatial resolutions, no proximity labeling platform with an intermediate spatial resolution has been developed (Fig. 3*A*). Such a platform would enable the study of biological structures on the low to mid micrometer scale. For example, cell-surface protein clusters critical for processes such as cell adhesion (43), neurotransmitter signaling (44), and immunoregulation (45–47) have been measured to range on this intermediate distance scale (70 to 200 nm), and platforms capable of selectively labeling their protein constituents are highly desired.

Although used extensively for photoaffinity cross-linking (48), aryl azides have only recently been showcased for their potential use in proximity labeling (49). Using visible light-driven organic photocatalysis, Zhang, Chen, and coworkers demonstrated visible light-mediated organophotocatalytic activation of aryl azide probes via proposed energy transfer from excited-state organic photocatalysts to catalytically generate aryl nitrene and ketenimine species as reactive probes. Using the mitochondrial specificity of their rhodamine photocatalyst to achieve intracellular localization, the authors were able to study the dynamic changes of the mitochondrial proteome under various stress conditions. However, no antigen-specific targeted proximity labeling was performed. Thus, we questioned if we could use our μMap platform to achieve targeted aryl azide-based proximity labeling. Importantly, we hypothesized that the intermediate solution half-life of the azide-derived ketenimine species (10 μs) (50) and relatively sluggish hydrogen atom transfer (HAT) of triplet nitrenes (51) could give rise to a platform with an intermediate degree of spatial selectivity (Fig. 3*B*).

First, we sought to identify the reactive intermediates generated under blue light-iridium photocatalysis. Upon subjecting model phenyl azide and tetrafluorophenyl azide substrates to blue light-induced photosensitization, we observed azobenzene and aniline products (*SI Appendix*, Fig. S3), strongly suggesting the in situ generation of triplet nitrene and nitrogen-centered radical species that can engage in HAT processes. Interestingly, in both cases, no ketenimine derivatives were identified, indicating that our iridium photocatalysis based platform offers different reactivity from acridinium-based systems. Using transient absorption spectroscopy and spectroelectrochemistry to elucidate the bimolecular mode of activation, we obtained direct evidence for an electron transfer, oxidative quenching pathway (*SI Appendix*). Finally, to confirm that these photocatalytically generated intermediates can cross-link with protein substrates, we performed in vitro labeling of BSA (*SI Appendix*, Fig. S4 and S5), observing a time-dependent increase in biotinylation.

To determine the radius of this method, we performed azide-μMap labeling studies with Biotin-PEG3-PhN_3 (**3**) and the commercially available Biotin-PEG3-PhF_4N_3 analog (**4**) on the reductionist model BSA system. When 5 mM of probe (**3**) or tetrafluoro analog (**4**) were irradiated on BSA-coated coverslips for 15 min at 450 nm wavelength, FWHMs of 119 ± 33 nm and 67 ± 23 nm were measured, respectively (Fig. 3 *C* and *D*).

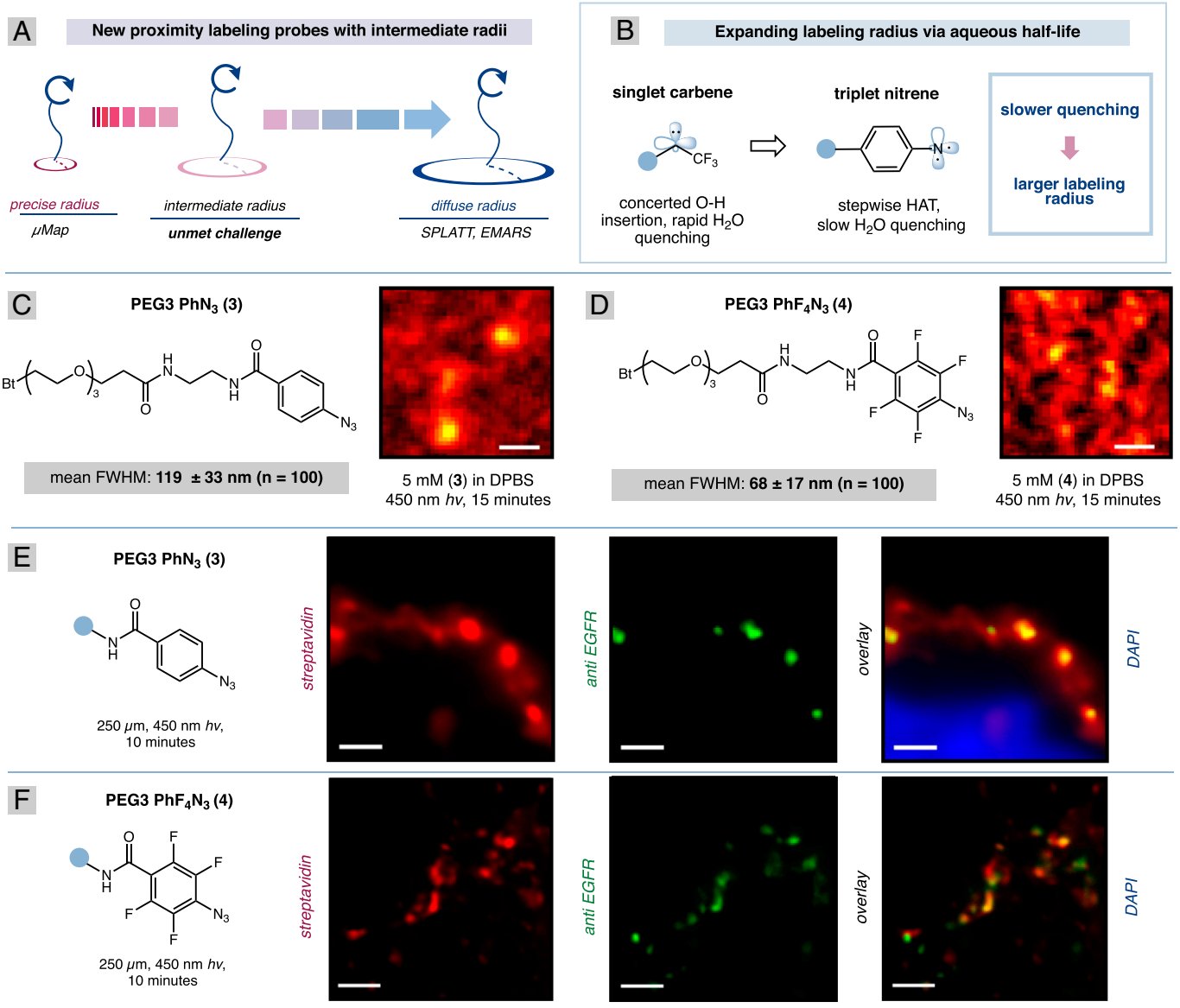

Fig. 3. (*A*) The development of a PLP that offers intermediate spatial resolution remains an unmet challenge. (*B*) Triplet nitrenes undergo quenching process at diminished rates compared to carbenes. (*C*) Measurement for the labeling radius of phenyl azide (**3**) using the BSA-coated coverslip model (scale bar, 200 nm). (*D*) Measurement for the labeling radius of F_4PhN_3 (**4**) using the BSA-coated coverslip model (scale bar, 200 nm). (*E*) Targeted labeling of the EGFR interactome on the surface of A549 cells using PhN_3 probe (**3**) (scale bar, 0.5 μm). (*F*) Targeted labeling of the EGFR interactome on the surface of A549 cells using PhN_3 probe (**4**) (scale bar, 0.5 μm).

We attribute the smaller labeling radius of the tetrafluoro analog to the increased reactivity of its corresponding intermediates, as fluorine-substituted aryl azide decomposition products show increased reactivity relative to their nonfluorinated congeners (16). We also observed this difference on the cell-surface EGFR interactome (Fig. 3 *E* and *F*), observing radial clusters of 147 ± 32 nm ($n = 30$) and 75 ± 20 nm ($n = 30$) for probes **3** and **4**, respectively. Notably, a greater irradiation time (10 min) was required to observe distinct labeling clusters on the cell surface.

Having confirmed that these phenyl azide probes provide an intermediate labeling radius via STED, we then sought to benchmark this novel spatial selectivity in the context of cell-surface targeting. Thus, we performed targeted labeling of the T-cell receptor (TCR) interactome using the μMap, PEG3 PhN_3 μMap, and peroxidase methods. Gratifyingly, the new intermediate-radius PLP afforded a greater number of known TCR interactors than μMap while maintaining high selectivity for the targeted interactome (*SI Appendix*, Figs. S9 and S10). Together, these data confirm the intermediate spatial selectivity of PEG3 PhN_3 μMap and showcase the utility of an intermediate radius platform for interactome mapping.

We next questioned if we could gain further control over spatial selectivity via simple structural modifications of the aryl azide probe. We mainly attribute differences in labeling radii across platforms to the characteristic solution half-life of each reactive intermediate. However, another physical parameter also governs the distance that a reactive species travels in solution: the species' diffusion coefficient. Thus, we wondered if we could truncate the labeling radius of a probe by simply decreasing the rate at which it can diffuse in solution (Fig. 4*A*). In this scenario, the species half-life would remain constant, but the average distance traveled over time would decrease due to reduced diffusion, resulting in a higher proportion of labeling events within close proximity of the catalyst and improved spatial resolution.

To test this hypothesis, we chose to extend the length of the PEG linker connecting the azide warhead to the biotin handle, as

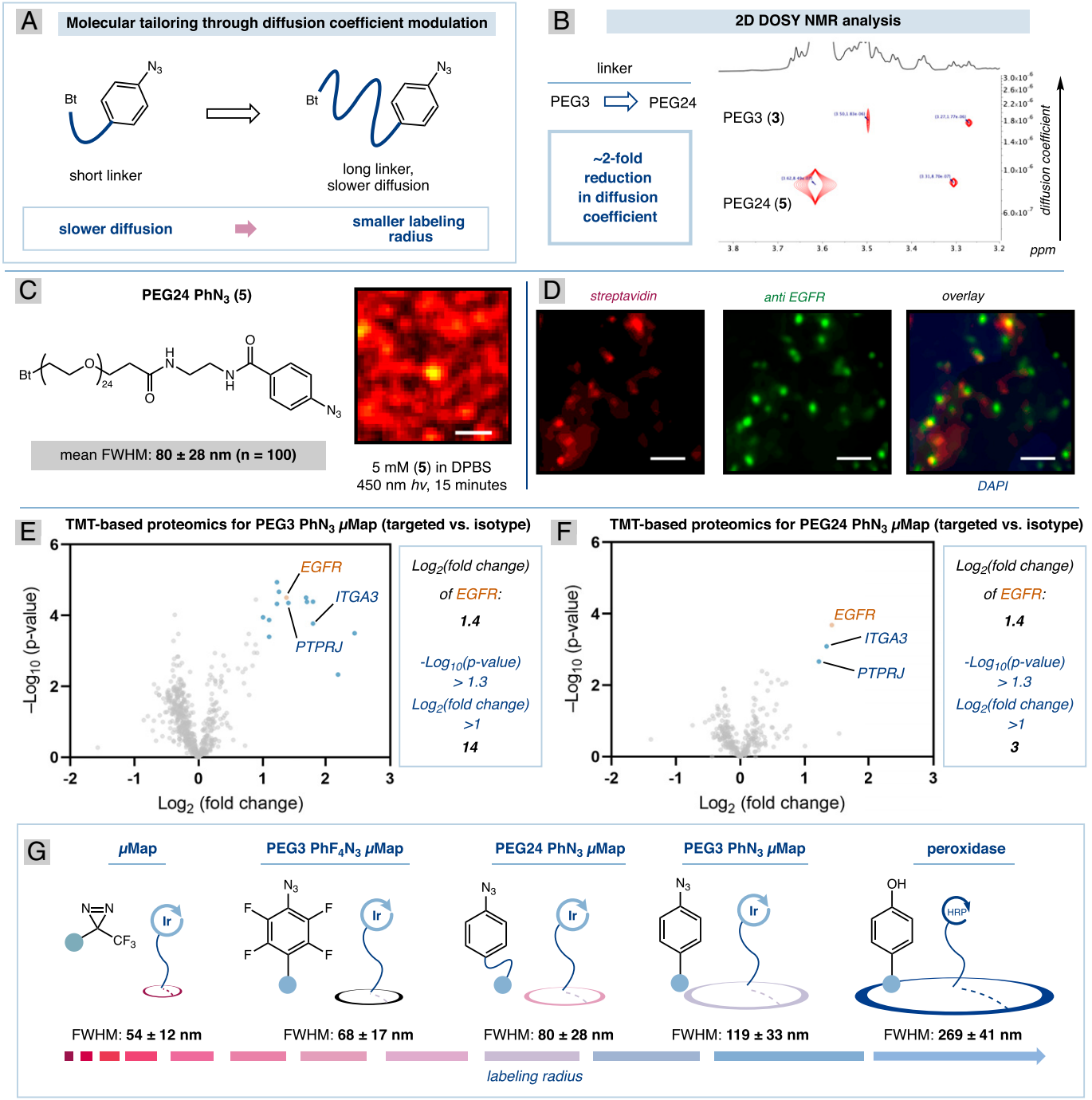

Fig. 4. (*A*) Truncating labeling radius by modulating the diffusion coefficient. (*B*) 2D DOSY NMR of a mixture of PEG3-PhN_3 (**3**) and PEG24-PhN_3 (**5**). Analysis of cross-peaks in the DOSY spectra reveals that the PEG24 analog has a ~1.6-fold reduced diffusion coefficient relative to PEG3. (*C*) STED image of BSA labeling on the surface of a coverslip with extended linker azide probe (**5**) reveals a labeling radius of 80 ± 28 nm. (*D*) Targeted cell-surface EGFR interactome labeling using PEG24 PhN_3 (**5**) reveals smaller clusters in the diffusion reduced labeling (scale bar, 0.5 μm). (*E*) TMT-based proteomics for PEG3 PhN_3-based μMap. (*F*) TMT-based proteomics for PEG24 PhN_3-based μMap. (*G*) Range of labeling radii measured across PLPs analyzed in this manuscript. These mean FWHM values (averages of 100 measurements) were calculated from clusters observed on BSA-coated coverslips.

PEG oligomers have been shown to have decreased diffusion coefficients with increasing molecular weights (52). If successful, this strategy could enable facile fine-tuning of the diffusion coefficient through modulation of PEG linker lengths. Thus, we prepared the PEG24 PhN_3 (**5**) as a diffusion-reduced analog of PEG3 PhN_3 (**3**). Indeed, using 2D Diffusion Ordered Spectroscopy (DOSY) NMR, we measured an approximately twofold decrease in diffusion of the PEG24 analog (**5**) relative to the PEG3 analog (**3**) (Fig. 4*B* and *SI Appendix*, Fig. S6); this result confirms that reduced diffusion can be achieved through this basic structural modification. Furthermore, when the PEG24 analog (**5**) was evaluated in our BSA model system, we observed radial clusters with an average FWHM of 80 ± 28 nm (Fig. 4*C*), a value ~1.5-fold smaller than the PEG3 analog. This key finding suggests that an increase in spatial precision can be achieved strictly through diffusional control. To evaluate whether this increase in spatial selectivity extends to the complex extracellular environment, we performed cell-surface labeling of the EGFR interactome. Consistent with the results measured on our model BSA interactome, we observed smaller cell-surface clusters for the PEG24 PhN_3

(**5**) (78 ± 23 nm, $n = 30$) in comparison to the truncated PEG3 analog (Figs. 3*E* vs. 4*D*). Finally, we sought to evaluate the impact of this reduced labeling radius on the enriched extracellular interactome of EGFR. Thus, our intermediate-precision PEG3-probe, **3**, tagged 14 enriched proteins, including four previously annotated interactors on the bioGRID database (Fig. 4*E*). Pleasingly, the higher-precision PEG24-probe, **5**, showed only two significant interactors (ITGA3, PTPRJ), both of which were present in the PEG3 probe (Fig. 4*F*). The overlap between the two analogous datasets suggests that by modulating the diffusion coefficient we are able to capture concentric EGFR interactomes of variable radii. Comparison of the enriched proteins from the azide datasets (**3** and **5**) with the hits from the phenoxyl radical (**2**) and carbene (**1**) probes showed an interesting correlation. Thus, the azide- and phenol-based probes shared a higher proportion of hits compared to the diazirine-based μMap system; 10 of the 14 PEG3 PhN_3 hits were also present in the HRP dataset (*SI Appendix*, Figs. S7 and S8 for Venn analysis). We attribute this phenomenon to the similar open shell reactivity profiles of the azide and phenol probes, both of which favor tyrosine labeling, in contrast to the residue-agnostic diazirine labeling (13, 53). Thus, the aryl azide and phenol PL platforms appear to show bias toward certain membrane proteins.

Conclusions

Using super-resolution microscopy, we have measured the extracellular labeling radii of state-of-the-art proximity labeling technologies and developed a PLP with unprecedented spatial resolution, adding to the repertoire of PLPs for interactome mapping (Fig. 4*G*). Dual-antibody targeting studies in a BSA model system suggest the μMap platform has an approximately fivefold smaller labeling radius compared to the peroxidase-based HRP platform. However, this difference does not account for the length of the dual antibody assembly itself, which we observed to be equal in length to that of the μMap labeling clusters. Thus, accounting for the tether length, the true radius of μMap is likely in the low-nm regime. Two aryl azide-μMap PLPs were developed and shown to possess intermediate labeling radii; these systems may prove useful in studying interactomes not aptly captured by μMap or HRP. Finally, while the varied aqueous half-lives of these reactive species—carbenes, nitrenes, and phenoxy radicals—present a complementary set of interactome mapping technologies, modulation of the diffusion coefficient provides a simple strategy to further tune the labeling radii of these probes. We expect that this general strategy will lead to the development of a menu of PLPs with varying degrees of labeling precision that will ultimately allow the tailored mapping of any interactome.

Materials and Methods

Photolabeling on Live A549 Cells for Imaging via STED Microscopy. Unless specified, all pelleting and washing of cells were performed at 300× g for 4 min at 4 °C. A549 cells were grown in Ham's F-12K medium (Gibco, 21127022) supplemented with 10% fetal bovine serum and 100 U/mL penicillin-streptomycin. Cells were dissociated from Nunc culture dishes (15 min incubation with TrypLE Express [Gibco, 12604-021] at 37 °C, quenched with complete DMEM), washed twice in 2 mL cold Dulbecco's phosphate buffered saline (DPBS), resuspended in cold DPBS at 3 million cells per milliliter, and transferred in 1 mL aliquots to 1.5 mL Eppendorf LoBind or Axygen Maxymum Recovery tubes. The cells were pelleted to remove the supernatant and resuspended in 300 μL of cold DPBS containing 2.5 μg of purified mouse (human *EGFR* antibody [clone EGFR.1, BD Biosciences, 555996 [or isotype antibody [clone MOPC-21, BD Biosciences, 556648]). The cells were incubated on a rotator for 30 min at 4 °C. After incubation, the cells were pelleted to remove the supernatant, washed twice with 300 μL cold DPBS, and resuspended in 300 μL of cold DPBS containing 2.5 μg of Ir-conjugated goat anti-mouse secondary antibody. The samples were incubated on a rotator for 30 min at 4 °C and pelleted to remove the supernatant. The cells were then washed twice with 1 mL of cold DPBS and resuspended in 300 μL of cold DPBS containing 250 μM of the specified probe (prepared from 250 mM stock in DMSO) in the *SI Appendix*, Table S2. The samples were placed in a 4 mL vial holder (PennPhD, PR-5-4-mL) and irradiated with 450 nm light using a PennPhD integrated photoreactor in a 4 °C cold room for the specified irradiation time in the photolabeling probe and irradiation timetable for imaging via STED microscopy (*SI Appendix*, Table S2). After irradiation, the cells were pelleted to remove the supernatant and washed twice with 300 μL cold DPBS. Each sample was resuspended in 500 μL of cold DPBS and added on top of poly-L-lysine coated coverslips and centrifuged at 400× g for 30 min at 4 °C in a Sorvall ST40 centrifuge (Thermo, 75004509) with acceleration/deceleration setting at 4. The supernatant was carefully aspirated, and the cells were fixed by adding 500 μL of 4% vol/vol paraformaldehyde (Pierce, 28906) in DPBS and incubating for 10 min at room temperature. After incubating, the cells on coverslips were carefully washed 2× with 500 μL room temperature DPBS, incubating for 5 min at room temperature for each wash. Coverslips were blocked at room temperature for 1 h with 300 μL 1% BSA, 22.52 mg/mL glycine in DPBST (0.1% Tween-20 in DPBS). After incubating, the supernatant was aspirated from the coverslip, and 200 μL of a solution of mouse α-EGFR antibody (Santa-Cruz, sc373746, 1:50 dilution) diluted in cold 1% BSA, 22.52 mg/mL glycine in DPBST was added. The coverslips were incubated overnight at 4 °C. After incubating, cells were washed 3× with 500 μL room temperature DPBS, incubating for 5 min at room temperature for each wash. The supernatant was removed, and the coverslips were incubated with 200 μL of a solution of goat anti-mouse secondary IgG Alexa Fluor 594 (Invitrogen A-11032, 1:1,000 dilution), Abberior Star 635 Streptavidin (Abberior, ST635-0120, 1:100; 1 mg/mL in TBST), and DAPI (0.5 μg/mL) diluted in cold 1% BSA, 22.52 mg/mL glycine in DPBST for 1 h. After incubating, cells were washed 3× with 500 μL room temperature DPBS, incubating 5 min at room temperature for each wash. One drop of ProLong Gold Anti-fade mountant (Invitrogen, P36934) was added to each glass microscopy slide (Lab Zap, B145-80). Using fine-point tweezers, each coverslip was placed on top of the mountant on the microscopy slide and allowed to dry at room temperature in the dark overnight before STED imaging on a Nikon eclipse Ti2 inverted confocal microscope (Nikon), equipped with a 100×/1.45 oil immersion objective (Nikon plan apo λ).

Data Availability. The data supporting the findings of this study are available within the article and its supporting information. Raw proteomic data can be accessed through the Proteomics Identification Database (PRIDE: https://www.ebi.ac.uk/pride/). All study data are included in the article and/or supporting information.

ACKNOWLEDGMENTS. This work was funded by the NIH National Institute of General Medical Sciences (R35-GM134897-02) and kind gifts from Merck, BMS, Pfizer, Janssen, Genentech, and Eli Lilly. We acknowledge the Princeton Catalysis Initiative for supporting this work. Mechanistic experiments, including transient absorption and UV-Vis spectroscopy, was supported by the Division and Chemical Sciences, Geosciences, Biosciences, and Office of Basic Energy Sciences of the U.S. Department of Energy (DOE) through grant DE-SC0019370. J.V.O. acknowledges the National Science Foundation Graduate Research Fellowship Program (DGE-1656466). Any opinions, findings, and conclusions or recommendations expressed in this material are those of the authors and do not necessarily reflect the views of the National Science Foundation. The authors thank Saw Kyin and Henry H. Shwe at the Princeton Proteomics Facility. Imaging was performed with support from the Confocal Imaging Facility, a Nikon Center of Excellence, in the Department of Molecular Biology at Princeton University.

1. Y. Iwai *et al.*, Involvement of PD-L1 on tumor cells in the escape from host immune system and tumor immunotherapy by PD-L1 blockade. *Proc. Natl. Acad. Sci. U.S.A.* **99**, 12293–12297 (2002).
2. S. H. Baumeister, G. J. Freeman, G. Dranoff, A. H. Sharpe, Coinhibitory pathways in immunotherapy for cancer. *Annu. Rev. Immunol.* **34**, 539–573 (2016).
3. A. Ribas, J. D. Wolchok, Cancer immunotherapy using checkpoint blockade. *Science* **359**, 1350–1355 (2018).
4. G. Lu *et al.*, The myeloma drug lenalidomide promotes the cereblon-dependent destruction of Ikaros proteins. *Science* **343**, 305–309 (2014).

5. D. E. Scott, A. R. Bayly, C. Abell, J. Skidmore, Small molecules, big targets: Drug discovery faces the protein-protein interaction challenge. *Nat. Rev. Drug Discov.* **15**, 533–550 (2016).
6. P. Filippakopoulos *et al.*, Selective inhibition of BET bromodomains. *Nature* **468**, 1067–1073 (2010).
7. R. M. Gulick *et al.*; MOTIVATE Study Teams, Maraviroc for previously treated patients with R5 HIV-1 infection. *N. Engl. J. Med.* **359**, 1429–1441 (2008).
8. M. Kozal *et al.*; BRIGHTE Trial Team, Fostemsavir in adults with multidrug-resistant HIV-1 infection. *N. Engl. J. Med.* **382**, 1232–1243 (2020).
9. A. Cuadrado *et al.*, Therapeutic targeting of the NRF2 and KEAP1 partnership in chronic diseases. *Nat. Rev. Drug Discov.* **18**, 295–317 (2019).
10. R. F. van Vollenhoven *et al.*; ORAL Standard Investigators, Tofacitinib or adalimumab versus placebo in rheumatoid arthritis. *N. Engl. J. Med.* **367**, 508–519 (2012).
11. L. A. Beck *et al.*, Dupilumab treatment in adults with moderate-to-severe atopic dermatitis. *N. Engl. J. Med.* **371**, 130–139 (2014).
12. W. Qin, K. F. Cho, P. E. Cavanagh, A. Y. Ting, Deciphering molecular interactions by proximity labeling. *Nat. Methods* **18**, 133–143 (2021).
13. H.-W. Rhee *et al.*, Proteomic mapping of mitochondria in living cells via spatially restricted enzymatic tagging. *Science* **339**, 1328–1331 (2013).
14. D. Z. Bar *et al.*, Biotinylation by antibody recognition–A method for proximity labeling. *Nat. Methods* **15**, 127–133 (2018).
15. J. S. Rees, X. Li, S. Perrett, K. S. Lilley, A. P. Jackson, Selective proteomic proximity labeling assay using tyramide (SPPLAT): A quantitative method for the proteomic analysis of localized membrane-bound protein clusters. *Curr. Prot. Protein Sci.* **80**, 19.27.1–19.27.18 (2015).
16. F. M. Fazal *et al.*, Atlas of subcellular RNA localization revealed by APEX-Seq. *Cell* **178**, 473–490.e26 (2019).
17. G. Wu, M. Nagala, P. R. Crocker, Identification of lectin counter-receptors on cell membranes by proximity labeling. *Glycobiology* **27**, 800–805 (2017).
18. X.-W. Li *et al.*, New insights into the DT40 B cell receptor cluster using a proteomic proximity labeling assay. *J. Biol. Chem.* **289**, 14434–14447 (2014).
19. J. S. Rees *et al.*, Identification of the cis-molecular neighbours of the immune checkpoint protein B7-H4 in the breast cancer cell-line SK-BR-3 by proteomic proximity labelling. *Int. J. Oncol.* **57**, 87–99 (2020).
20. J. Li *et al.*, Cell-surface proteomic profiling in the fly brain uncovers wiring regulators. *Cell* **180**, 373–386.e15 (2020).
21. B. T. Lobingier *et al.*, An approach to spatiotemporally resolve protein interaction networks in living cells. *Cell* **169**, 350–360.e12 (2017).
22. S. Grainger *et al.*, EGFR is required for Wnt9a-Fzd9b signalling specificity in haematopoietic stem cells. *Nat. Cell Biol.* **21**, 721–730 (2019).
23. L. K. Folkes, M. Trujillo, S. Bartesaghi, R. Radi, P. Wardman, Kinetics of reduction of tyrosine phenoxyl radicals by glutathione. *Arch. Biochem. Biophys.* **506**, 242–249 (2011).
24. V. Hung *et al.*, Proteomic mapping of the human mitochondrial intermembrane space in live cells via ratiometric APEX tagging. *Mol. Cell* **55**, 332–341 (2014).
25. J. B. Geri *et al.*, Microenvironment mapping via Dexter energy transfer on immune cells. *Science* **367**, 1091–1097 (2020).
26. M. Ke *et al.*, Spatiotemporal profiling of cytosolic signaling complexes in living cells by selective proximity proteomics. *Nat. Commun.* **12**, 71 (2021).
27. Y. Zhou *et al.*, Expanding APEX2 substrates for proximity-dependent labeling of nucleic acids and proteins in living cells. *Angew. Chem. Int. Ed. Engl.* **58**, 11763–11767 (2019).
28. G. Mayer, M. Bendayan, Amplification methods for the immunolocalization of rare molecules in cells and tissues. *Prog. Histochem. Cytochem.* **36**, 3–85 (2001).
29. J. D. Martell *et al.*, Engineered ascorbate peroxidase as a genetically encoded reporter for electron microscopy. *Nat. Biotechnol.* **30**, 1143–1148 (2012).
30. A. Meister, Glutathione metabolism and its selective modification. *J. Biol. Chem.* **263**, 17205–17208 (1988).
31. S. B. Zimmerman, S. O. Trach, Estimation of macromolecule concentrations and excluded volume effects for the cytoplasm of *Escherichia coli*. *J. Mol. Biol.* **222**, 599–620 (1991).
32. S. B. Zimmerman, A. P. Minton, Macromolecular crowding: biochemical, biophysical, and physiological consequences. *Annu. Rev. Biophys. Biomol. Struct.* **22**, 27–65 (1993).
33. N. Kotani *et al.*, Biochemical visualization of cell surface molecular clustering in living cells. *Proc. Natl. Acad. Sci. U.S.A.* **105**, 7405–7409 (2008).
34. S. J. Sahl, S. W. Hell, S. Jakobs, Fluorescence nanoscopy in cell biology. *Nat. Rev. Mol. Cell Biol.* **18**, 685–701 (2017).
35. T. Müller, C. Schumann, A. Kraegeloh, STED microscopy and its applications: New insights into cellular processes on the nanoscale. *ChemPhysChem* **13**, 1986–2000 (2012).
36. H. C. Berg, *Random Walks in Biology* (Princeton University Press, 1993).
37. R. Oughtred *et al.*, The BioGRID database: A comprehensive biomedical resource of curated protein, genetic, and chemical interactions. *Protein Sci.* **30**, 187–200 (2021).
38. S. Foerster *et al.*, Characterization of the EGFR interactome reveals associated protein complex networks and intracellular receptor dynamics. *Proteomics* **13**, 3131–3144 (2013).
39. J. Li *et al.*, Perturbation of the mutated EGFR interactome identifies vulnerabilities and resistance mechanisms. *Mol. Syst. Biol.* **9**, 705 (2013).
40. J. Tong, P. Taylor, M. F. Moran, Proteomic analysis of the EGFR interactome and post-translational modifications associated with receptor endocytosis in response to EGF and stress. *Mol. Cell. Proteomics* **13**, 1655–1658 (2014).
41. H.-B. Guo, H. Johnson, M. Randolph, I. Lee, M. Pierce, Knockdown of GnT-Va expression inhibits ligand-induced downregulation of the epidermal growth factor receptor and intracellular signaling by inhibiting receptor endocytosis. *Glycobiology* **19**, 547–559 (2009).
42. E. L. Huttlin *et al.*, Dual proteome-scale networks reveal cell-specific remodeling of the human interactome. *Cell* **184**, 3022–3040.e28 (2021).
43. A. Cambi *et al.*, Organization of the integrin LFA-1 in nanoclusters regulates its activity. *Mol. Biol. Cell* **17**, 4270–4281 (2006).
44. H. D. MacGillavry, Y. Song, S. Raghavachari, T. A. Blanpied, Nanoscale scaffolding domains within the postsynaptic density concentrate synaptic AMPA receptors. *Neuron* **78**, 615–622 (2013).
45. B. F. Lillemeier *et al.*, TCR and Lat are expressed on separate protein islands on T cell membranes and concatenate during activation. *Nat. Immunol.* **11**, 90–96 (2010).
46. S. V. Pageon *et al.*, Superresolution microscopy reveals nanometer-scale reorganization of inhibitory natural killer cell receptors upon activation of NKG2D. *Sci. Signal.* **6**, ra62 (2013).
47. Y. S. Hu, H. Cang, B. F. Lillemeier, Superresolution imaging reveals nanometer-and micrometer-scale spatial distributions of T-cell receptors in lymph nodes. *Nat. Proc. Acad. Sci.* **113**, 720–17206 (2016).
48. D. P. Murale, S. C. Hong, M. M. Haque, J. S. Lee, Photo-affinity labeling (PAL) in chemical proteomics: A handy tool to investigate protein-protein interactions (PPIs). *Proteome Sci.* **15**, 14 (2017).
49. H. Wang *et al.*, Selective mitochondrial protein labeling enabled by biocompatible photocatalytic reactions inside live cells. *JACS Au* **1**, 1066–1075 (2021).
50. M. S. Rizk, X. Shi, M. S. Platz, Lifetimes and reactivities of some 1,2-didehydroazepines commonly used in photoaffinity labeling experiments in aqueous solutions. *Biochemistry* **45**, 543–551 (2006).
51. G. A. Gohar, M. S. Platz, A laser flash photolysis study of diphenylphosphoryl azide. Kinetics of singlet and triplet nitrene processes. *J. Phys. Chem. A* **107**, 3704–3707 (2003).
52. K. Shimada, H. Kato, T. Saito, S. Matsuyama, S. Kinugasa, Precise measurement of the self-diffusion coefficient for poly(ethylene glycol) in aqueous solution using uniform oligomers. *J. Chem. Phys.* **122**, 244914 (2005).
53. F. Kotzyba-Hilbert, I. Kapfer, M. Goeldner, Recent trends in photoaffinity labeling. *Angew. Chem. Int. Ed. Engl.* **34**, 1296–1312 (1995).